Materials Today Communications 52 (2026) 115134

Contents lists available at ScienceDirect

Materials Today Communications

journal homepage: www.elsevier.com/locate/mtcomm

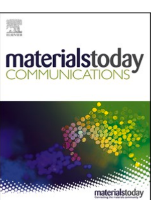

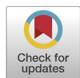

Orthorhombic ZrO_2 thin films via atomic layer deposition from tris(dimethylamino)cyclopentadienyl zirconium and water

Basit Ali [a,1], Ramin Ghiyasi [a,1], Joona Pekkanen [a], Mika Lastusaari [b], Maarit Karppinen [a,*]

[a] Department of Chemistry and Materials Science, Aalto University, P.O. Box 16100, Aalto FI-00076, Finland
[b] Department of Chemistry, University of Turku, Turku 20014, Finland

ARTICLE INFO

Keywords:
Atomic layer deposition
Thin films
Orthorhombic ZrO_2
Ferroelectrics

ABSTRACT

Different zirconium dioxide phases exhibit attractive functional properties, making them suitable for various applications. Among these, orthorhombic o-ZrO_2 is of particular interest due to its distinctive ferroelectric behavior. However, synthesizing phase-pure o-ZrO_2 thin films has remained challenging. Here, we demonstrate a robust water-based atomic layer deposition (ALD) process for o-ZrO_2 thin films using tris(dimethylamino) cyclopentadienyl zirconium as the precursor. The films were characterized by grazing-incidence X-ray diffraction (GIXRD), X-ray reflectivity (XRR), ellipsometry, X-ray photoelectron spectroscopy (XPS), atomic force microscopy (AFM), and photoluminescence (PL) techniques. In the deposition temperature range of 225–250 °C, the process yielded nearly phase-pure o-ZrO_2 films with a growth-per-cycle (GPC) of 0.5 Å/cycle, whereas above 275 °C, monoclinic m-ZrO_2 films were obtained with GPC of 0.6 Å/cycle. Interestingly, longer relaxation times during deposition were found to affect the growth rate, which we tentatively attributed to changes in crystallization dynamics and stabilization of different orthorhombic space groups.

1. Introduction

Zirconium dioxide is an attractive material for various emerging applications ranging from microelectronics to protective coatings in battery applications, due to its characteristic thermal, dielectric, electrical, and catalytic properties [1–3]. Under conventional synthesis conditions, ZrO_2 is obtained in multiple crystalline forms, including monoclinic (m-ZrO_2) and tetragonal (t-ZrO_2) [4,5], while the metastable orthorhombic (o-ZrO_2) phase is stabilized in powder form only under high-pressure conditions [6,7]. Due to such challenges, the unique properties of o-ZrO_2 have not been extensively studied [8,9]. Recently, the o-ZrO_2 phase has gained significant attention owing to its ferroelectric properties. Similar to o-HfO_2, the polar o-ZrO_2 phase with space group *Pca2₁* exhibits unconventional ferroelectric behavior [10–15]. Most excitingly, the capability of o-ZrO_2 to maintain its ferroelectricity in a wider thickness range without any doping [16,17], as well as its lower crystallization temperature compared to HfO_2 [18], are highly favorable factors considering its future applications, e.g., in memory devices [19,20]. Moreover, zirconium is 50 times more Earth-abundant than hafnium.

Atomic layer deposition (ALD) is a state-of-the-art technique that enables precise control during the fabrication of high-quality thin films, making it ideal for diverse applications, particularly in electronics [21–25]. So far, various ALD processes have been developed for ZrO_2 based on different zirconium precursors ($ZrCl_4$, ZrI_4, $Zr(thd)_4$, $Cp_2Zr(CH_3)_2$, Cp_2ZrCl_2, $Cp_2Zr(CH_3)_2$, $Zr[OC(CH_3)_3]_4$, $[Zr(C(CH_3)_3)_2(dmae)_2]_2$, $Zr[OC(CH_3)_3]_4$) and oxygen sources (H_2O, H_2O-H_2O_2, O_3, O_2) as listed in Table 1 [26–34,39]. However, these processes have yielded either amorphous films or, in the case of crystalline films, t-ZrO_2 or m-ZrO_2 as the main phase; in the studies so far reported, the o-ZrO_2 phase has been either not seen at all or detected only as a minority phase. Developing a new ALD process capable of producing phase-pure o-ZrO_2 films would significantly advance the potential application of o-ZrO_2 as a ferroelectric component in electronic devices.

Here we present a robust water-based ALD process for ZrO_2 and evaluate its capability to produce different ZrO_2 phases, particularly the orthorhombic o-ZrO_2 phase. In this process, tris(dimethylamino)cyclopentadienyl zirconium ($CpZr(NMe2)_3$) is utilized as the zirconium source; see Fig. 1 for its molecular structure. In a patent from the year

* Corresponding author at: Department of Chemistry and Materials Science, School of Chemical Engineering, Aalto University, P.O. Box 16100, Aalto FI-00076, Finland.
E-mail address: maarit.karppinen@aalto.fi (M. Karppinen).
[1] Equal contribution.

https://doi.org/10.1016/j.mtcomm.2026.115134
Received 26 November 2025; Received in revised form 2 April 2026; Accepted 7 April 2026
Available online 7 April 2026
2352-4928/© 2026 The Author(s). Published by Elsevier Ltd. This is an open access article under the CC BY license (http://creativecommons.org/licenses/by/4.0/).

Table 1
Reported ALD processes with complete process optimization for ZrO_2 thin films together with the resultant ZrO_2 phase composition.

Zr precursor / Co-reactant	ALD temp. window (°C): GPC (Å/c)	Substrate	Product / Temp. range	Ref.
$ZrCl_4$ / H_2O	500: 0.53	SL glass	amor., m* or t * /500	[26]
	280–350: 1.0 380–400: 5.0	SL glass	t / 275–350, m & t / 375 – 450	[27]
	400–600: 1.1	Si	c / 210, t & m_{TD}* / 300–600	[28]
ZrI_4 / H_2O- H_2O_2	325–500: 0.06	Si	c & m_{TD}* / 250–375, t & m_{TD} / 300–500	[29]
$Zr(thd)_4$ / O_3	375 - 500: 0.24	Si	m & o / 300, 375	[30]
$Cp_2Zr(CH_3)_2$ / O_3	310 - 500: 0.55	Si	m & o* / 300, 350	[30]
Cp_2ZrCl_2 / O_3	275 - 500: 0.53	Si	m & o* / 300, 350	[30]
$Cp_2Zr(CH_3)_2$ / H_2O	275–350: 0.43	Si	m & o* / 350–400	[31]
$Zr[OC(CH_3)_3]_4$ / H_2O	150–180: 1.2 250–280: 0.07	SL glass	amorphous	[32]
$[Zr(C(CH_3)_3)_2(dmae)_2]_2$ / H_2O	No ALD window	SL glass	amorphous	[33]
$Zr[OC(CH_3)_3]_4$ / O_2 plasma	No ALD window	Si	amorphous	[34]
TDMAZr / O_3	200 – 250: 1.25	Si	c, m & o / 150–350	[39]
$CpZr(NMe2)_3$ / H_2O	200–250: 0.5 275–300: 0.6	Si	o / 225–250, m & o* / 275–325	This work

* = minor phase; TD = thickness dependent.

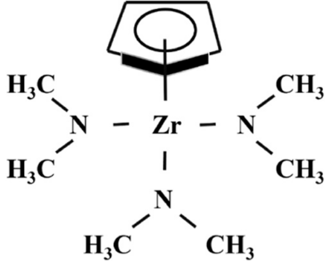

Fig. 1. Molecular structure of $CpZr(NMe2)_3$ precursor.

2014, $CpZr(NMe2)_3$ was highlighted as a highly volatile and thermally stable precursor [35]. It was later utilized in a PEALD (plasma-enhanced ALD) process [36], as well as in an ozone-based thermal ALD process [37], both of which were conducted at high deposition temperatures, i.e., 300 and 350 °C, respectively. However, the ALD process parameters used and their optimization were not reported; likewise, the crystal structure of the resultant thin films was not thoroughly investigated at various deposition temperatures.

The possible reaction route for the $CpZr(NMe2)_3$ plus water deposition process is as follows:

First half-cycle:

$$2Si{-}OH + CpZr(NMe_2)_3\ (g) \rightarrow Si{-}O{-}Zr(NMe_2)Cp{-}O{-}Si + 2HNMe_2\ (g)$$

Second half-cycle:

$$Si{-}O{-}Zr(NMe_2)Cp{-}O{-}Si + 2H_2O\ (g) \rightarrow Si{-}O{-}Zr(OH)_2{-}O{-}Si + HNMe_2\ (g) + CpH\ (g)$$

Overall deposition reaction:

$$CpZr(NMe_2)_3\ (g) + 2H_2O\ (g) \rightarrow ZrO_2\ (s) + 3HNMe_2\ (g) + CpH\ (g)$$

Interestingly, for HfO_2 a similar ALD process based on $CpHf(NMe_2)_3$ and H_2O has been employed but at much higher deposition temperatures, i.e., 305–410 °C [9]. This difference in deposition temperatures can be explained by the higher charge density of hafnium, leading to stronger metal-organic bonding and higher thermal stability.

2. Experimental

The ZrO_2 thin films were deposited from tris(dimethylamino)cyclopentadienyl zirconium ($CpZr(NMe2)_3$; Dockweiler Chemicals GmbH, Germany; > 99%) and H_2O (distilled water) using a commercial ALD reactor (Picosun Oy R-100). Nitrogen (99.9%) was used as a carrier and purging gas, and the pressure was kept at 2–3 mbar in the reactor during the depositions. All the depositions were made on Si(100) wafers with a native SiO_2 layer (Okmetic Ltd.; 2 ×2 cm^2) without any pretreatments. The $CpZr(NMe2)_3$ precursor was heated at 110 °C for the vaporization, and the $CpZr(NMe2)_3$ + H_2O process was investigated in the deposition temperature range from 200 to 325 °C. The precursor heating temperature of 110 °C was initially selected based on the information from the chemical supplier, and then adjusted by searching for the lowest heating temperature at which stable vapor pressure and reproducible mass transport were achieved; the chosen temperature is also in line with the thermogravimetric data reported for $CpZr(NMe2)_3$ in literature [38]. The precursor pulse length optimization was performed at the deposition temperature of 250 °C, by varying the $CpZr(NMe2)_3$ and H_2O pulse lengths between 0.4 and 1.0 s, and 0.1 and 0.4 s, respectively, while the N_2 purge length was fixed to 3 s after both precursor pulses. In addition to these conventional ALD cycles in which the total cycle time was typically 6.8 s (= 0.6 s + 3 s + 0.2 s + 3 s), we carried out a few depositions at 230, 240 and 250 °C using an "elongated-cycle" scheme to investigate the influence of extended surface relaxation times on the crystallization process; in these depositions the total cycle time was 10.8 s (= 0.6 s + 5 s + 0.2 s + 5 s) or 20.8 s (= 0.6 s + 10 s + 0.2 s + 10 s).

The film thicknesses were determined primarily by X-ray reflectivity (XRR; Rigaku SmartLab diffractometer; 45 kV and 200 mA) measurements; for some of the samples, the film thickness was additionally determined using a spectroscopic ellipsometer (Horiba UVISEL Plus; 200 ms integration time, step size 5 nm, spot size 1 mm, incident angle 70°). The obtained data were analyzed by Horiba's DeltaPsi2 and X'Pert reflectivity software, respectively. To obtain optical constants, the ellipsometry data were freely fitted utilizing a spectroscopic model called New Amorphous [40–42]. The same X-ray diffractometer applied in XRR mode was also used for the grazing incident X-ray diffraction (GIXRD; CuKα radiation, 1.54056 Å and 1.54441 Å) mode to investigate the crystallinity and phase composition of the films; the GIXRD data were analyzed by Match 4 software. The film surface roughnesses were evaluated from the XRR data and also measured by atomic force microscopy (AFM; Bruker Dimension Icon AFM) on 2 × 2 μm^2 in ScanAsyst imaging mode with scan rate of 1 Hz and 512-pixels scan resolutions.

The chemical composition was investigated for three representative ZrO_2 thin films (deposited at 200, 250, and 325 °C) by X-ray photoelectron spectroscopy (XPS; Kratos Analytical AXIS Ultra, with DLD detector) using a monochromated $Al_{K\alpha}$ X-ray source (1486.7 eV) run at 100 W. No sputtering was carried out on the samples, and the collection angle was 90 ° for all measurements. The XPS was operated by an Omicron Argus spectrometer at a 20 eV pass energy, and the obtained data were analyzed by the CasaXPS software package.

Photoluminescence (PL) spectra were collected using an Edinburgh Instruments FLS1000 spectrometer equipped with a continuous wave 450 W Xe arc lamp and a PMT-900 photomultiplier tube, operated at an excitation wavelength of 255 nm. A Standa BS3 filter was used on the

emission side to prevent reflected excitation from reaching to the detector.

3. Results and discussion

3.1. ALD process optimization

For the ALD process optimization, we systematically investigated the effects of the following process parameters on the ZrO_2 film growth: deposition temperature (phase composition and so-called ALD window), precursor pulse lengths (surface saturation), and number of ALD cycles applied (linearity of the film growth); the resulting changes in the film thickness were monitored with both XRR and ellipsometry measurements, to obtain the growth-per-cycle (GPC) values (= film thickness divided by ALD cycle number). The XRR results are presented in Fig. 2 and the ellipsometry results in Supporting Info, Figure S1; the trends observed are essentially parallel but it should be noted that – like here – XRR and ellipsometry may yield slightly different thickness values, explained by the fact that they probe different properties, i.e. electron density changes or optical constant differences at the film/substrate interface, respectively.

From our preliminary tests, we observed that the $CpZr(NMe2)_3$ + H_2O process yielded highly crystalline and nearly phase-pure o-ZrO_2 films at 250 °C; hence, the deposition temperature was fixed to 250 °C for the systematic precursor pulse length optimization experiments. The films were grown with 1000 ALD cycles in each case, and the N_2 purge time was set to 3 s for both precursors to assure – based on our previous experience on related processes – that the purge pulse is long enough to remove any excess precursor and byproduct molecules from the gas phase; note that we also confirmed for one sample that the GPC value remained unaffected when we increased the purge time from 3 s to 6 s. From Figs. 2a and 2b, the surface saturation condition is reached for the $CpZr(NMe2)_3$ precursor with a pulse length of 0.6 s, while for the water pulse, a shorter pulse length of 0.2 s was enough for the saturation. These findings confirm the self-limiting behavior of the $CpZr(NMe2)_3$ + H_2O process, which is an inherent criterion of an ideal ALD process.

Subsequently, we confirmed the film growth linearity, which is another important characteristic of a well-behaving ALD process. In these experiments, the aforementioned optimized precursor and purge pulse lengths, i.e. 0.6 s / 3 s / 0.2 s /3 s, were applied. From Fig. 2c, it is seen that the film thickness increases in an essentially linear manner when the number of cycles is increased from 200 to 2000. From the slope of the line, the average GPC value was obtained at 0.51 ± 0.02 Å/cycle. Additionally, the fact that the fitted line does not intersect the origin (zero thickness at zero cycles) but instead extrapolates to a slightly negative thickness indicates a small nucleation delay. This delay is

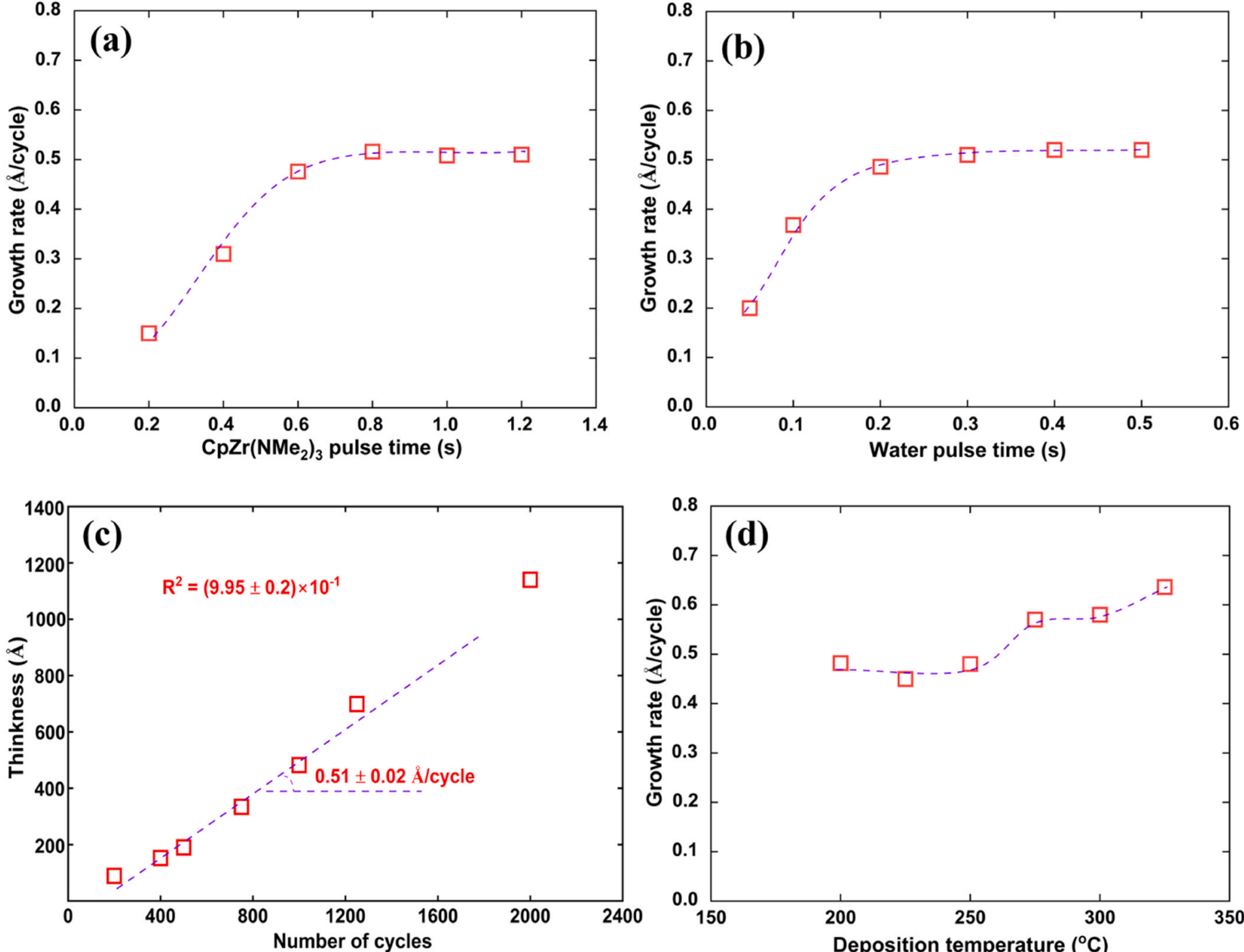

Fig. 2. ALD process optimization based on XRR data for the film thickness/GPC value: GPC versus (a) $CpZr(NMe2)_3$ precursor, and (b) water pulse lengths; (c) film thickness versus number of ALD cycles; (d) GPC versus deposition temperature. In all these experiments the fixed parameters were (when one of the parameters was varied): deposition temperature 250 °C, number of ALD cycles 1000, and pulse/purge sequence 0.6 s / 3 s / 0.2 s /3 s.

minor though, as the film has already reached ca. 9 nm thickness by 200 cycles.

Finally, we investigated the film growth at different deposition temperatures in the 200–325 °C range, as shown in Fig. 2d. In preliminary experiments, we found that some deposition occurred even at 180 °C, but the resulting films were non-uniform and were therefore excluded from further investigations. The upper temperature limit of 325 °C was defined by our reactor limitations. From Fig. 2d, two distinct GPC plateaus (or ALD windows) are seen, around 200–250 °C (GPC ca. 0.5 Å/cycle) and 275–325 °C (GPC ca. 0.6 Å/cycle). These observed differences in the GPC value within the two plateaus likely originate from the different crystal structures of the ZrO_2 product, as discussed in detail in the subsequent section.

3.2. Film characterization

To investigate the phase composition of the films deposited at different temperatures ranging from 200 to 325 °C, GIXRD patterns were acquired, as presented in Fig. 3. So far in literature, the most common experimentally verified crystal structures for ZrO_2 are as follows: monoclinic ($P2_1/c$: JCPD 96–152–8985), orthorhombic (Pbca, $Pca2_1$ & Pnma: JCPD 04–007–0952, 96–900–9920, 00–049–1746), tetragonal ($P4_2/nmc$: JCPD 96–152–5706), and cubic ($Fm\bar{3}m$: JCPD 96–152–1754). Note that for the orthorhombic phase, several alternative space groups have been reported, but it is truly challenging if not impossible to distinguish between these different space groups based on standard diffraction techniques. In addition to GIXRD, other research groups have also utilized Raman spectroscopy for phase determination [37]; however, our efforts were not successful.

The film deposited at 200 °C was predominantly amorphous, the GIXRD pattern showing only a few weak diffraction peaks. With increasing deposition temperature, the degree of crystallinity systematically increased, such that up to 250 °C the diffraction peaks and their positions remained the same; essentially all the diffraction peaks seen for these films could be indexed according to the orthorhombic ($Pca2_1$) o-ZrO_2 structure, except the weak peak around 28.4° which could be the main diffraction peak due to m-ZrO_2. Then, upon a further increase in the deposition temperature the crystal structure clearly changed to the monoclinic m-ZrO_2 ($P2_1/c$) structure. The volume per formula unit ($V_{f.u.}$) for the monoclinic m-ZrO_2 structure is larger (35.4 $Å^3$/f.u.) compared to the orthorhombic o-ZrO_2 structure (34.2 $Å^3$/f.u. for $Pca2_1$, 33.9 $Å^3$/f.u. for Pbca, 31.4 $Å^3$/f.u. for Pnma); interestingly, this is well in line with the higher GPC values observed for the m-ZrO_2 films (higher deposition temperature range in Fig. 2d). We also like to note that the peak positions observed for the two phases are in line with those previously reported in literature [43,44]: 24.08° (m-ZrO_2), 24.44° (o-ZrO_2), 28.39° (m-ZrO_2), 30.36° (o-ZrO_2), 31.55° (m-ZrO_2), 34.6° (m-ZrO_2), 35.48° (o-ZrO_2), 38.9° (m-ZrO_2), 41.2° (m-ZrO_2), 45.05° (m-ZrO_2), 59.96° (m-ZrO_2), 60.61° (o-ZrO_2), 62.81° (m-ZrO_2), 63.25° (o-ZrO_2), and 66.03° (m-ZrO_2). Finally, we confirmed for the 250 °C deposited samples the o-ZrO_2 phase stability in relation to the film thickness; the GIXRD patterns shown in Figure S2 (Supporting info) reveal no visible thickness-dependent differences.

During the process development stage, the films were deposited already with a relatively long overall ALD cycle duration of 6.8 s (0.6 s + 3 s + 0.2 s + 3 s) for which the pulse and purge durations were considered sufficient to supply the precursors and remove the process residuals. However, we wanted to investigate the influence of significantly elongated deposition cycles on the crystallization of the films through relaxation time enhancement. For this, we carried out additional depositions at 240 and 250 °C (i.e., at the two deposition temperatures yielding the most crystalline orthorhombic phases) and increased the total cycle time by threefold from 6.8 to 20.8 s (= 0.6 s + 10 s + 0.2 s + 10 s). As anticipated, the longer cycle time resulted in a higher degree of crystallinity, see Fig. 4. However, in the sample deposited at 250 °C, it also resulted in a partial phase change from orthorhombic to monoclinic, while the sample deposited at 240 °C was highly crystalline and showed only traces of the m-ZrO_2 phase. Most interestingly, the GPC value seemed to be significantly lower (ca. 0.35 Å/cycle) for this 240 °C sample compared to the values obtained for the films deposited with the "optimized" shorter cycle time (ca. 0.5 Å/cycle) in the "orthorhombic" deposition temperature range of 225 – 250 °C. Because of the higher degree of crystallinity, the films deposited with the elongated cycle time were exceptionally rough, and therefore their thicknesses were challenging to determine with XRR. To corroborate the result, we carried out additional depositions at 230 and 240 °C using an intermediate overall cycle duration of 10.8 s (= 0.6 s + 5 s + 0.2 s + 5 s); the GPC values determined by ellipsometry measurements were 0.37 and 0.36 Å/cycle, respectively. The lower growth rate values could be explained as a consequence of the previously reported effect of longer purge duration on the growth rate due to desorption of attached precursors on the surface [45], or due to the higher degree of crystallinity and thus a somewhat higher density of the growing o-ZrO_2 film. Finally, a third plausible reason or contributing factor could be stabilization of a slightly different crystal structure with a lower $V_{f.u.}$, i.e. o-ZrO_2 structure with space group Pbca (33.9 $Å^3$/f.u) or Pnma (31.4 $Å^3$/f.u.), instead of $Pca2_1$ (34.2 $Å^3$/f.u.) [6,46,47]. However, all these suggested explanations remain tentative and require validation

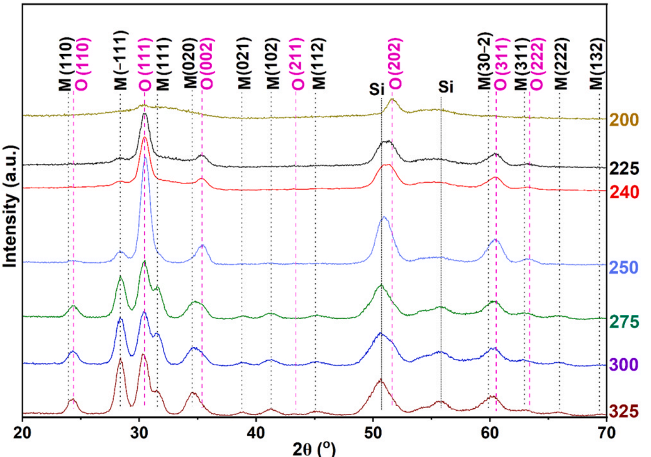

Fig. 3. GIXRD patterns for ZrO_2 films deposited at various temperatures, using the following deposition parameters: number of ALD cycles 1000, and pulse/purge sequence 0.6 s / 3 s / 0.2 s /3 s; Si stands for silicon substrate.

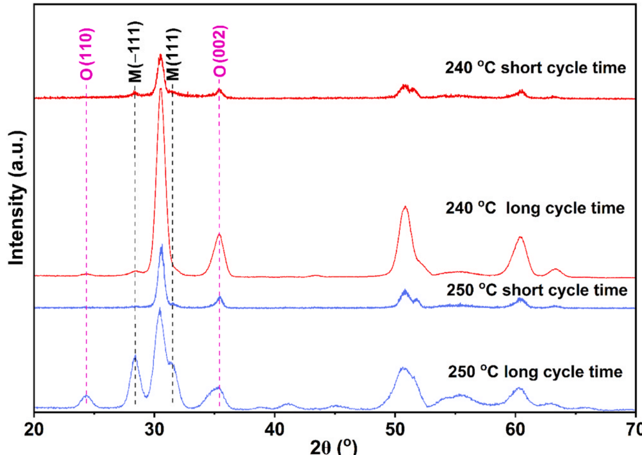

Fig. 4. GIXRD patterns for the ZrO_2 thin films deposited at 240 and 250 °C with the shorter (6.8 s) and longer (20.8 s) cycle durations; the number of ALD cycles applied was 1000.

through complementary analytical methods.

The XRR patterns for the ZrO_2 films deposited (with the optimized/shorter cycle duration) at temperatures from 200 to 325 °C are shown in Fig. 5. From the critical angles obtained from the XRR patterns [48], the film densities were calculated at ca. 4.6 g/cm^3 for these films (ideal bulk density of ZrO_2: 5.68 g/cm^3). It should be emphasized that the difference seen here between the thin-film and ideal-bulk density values is rather typical for high-quality pinhole-free ALD thin films [43], e.g. for HfO_2 films 7.7 g/cm^3 versus 9.6 g/cm^3 [49]. Most of the samples exhibited very similar XRR patterns except the two grown at 240 and 250 °C, which appeared significantly rougher compared to the others (oscillations weaker in magnitude). Similarly, AFM measurements yielded higher roughness values for these two thin films, ca. 4.1 nm in comparison to the ca. 2.5 nm for the other samples (Fig. 6, Table 2). Tentatively, we attribute the anomalous roughness values of the 240 and 250 °C samples to their small but emerging two-phase character, even though the m-ZrO_2 phase is below the detection limit of GIXRD in the 240 °C sample. The AFM images, moreover, revealed that the coatings were appreciably uniform and pinhole-free, like also expected based on other characterizations and visual observations.

To gain further understanding of the film composition, XPS spectra were collected for representative samples; the XPS core-level spectra of films grown at 200, 250, and 325 °C (Fig. 7) indicate a single ZrO_2 lattice doublet of Zr 3d with $3d_{5/2} = 182.0 \pm 0.1$ eV, 2.39 eV spin–orbit splitting, almost equal FWHM, and a $3d_{5/2}/3d_{3/2}$ area ratio of 3:2, which are consistent with fully oxidized Zr^{4+}. No other phases, such as suboxides, were detected. In the O 1 s region, the lattice O^{2-} appears at 529.9 ± 0.2 eV, while the –OH/oxygen defect peak is seen at 531.3–531.7 eV [50–52]. The –OH fraction systematically decreases with increasing deposition temperature, from 32% at 200 °C to 18% at 250 °C, and 17% at 325 °C, indicating increasing dehydroxylation. The C 1 s region is dominated by adventitious C–C/C–H with a minor O–C–/C═O feature at 288.5–288.7 eV and 7–10% fraction, the latter being attributed to surface carboxylate/carbonate-like species formed upon ambient exposure of the hydroxylated oxide surface [53,54]. Overall, the spectra confirm the expected ZrO_2 phase across the sample series with no other Zr formations or significant contaminations (see also the full XPS survey spectra in SI, Figure S3), with reduced surface hydroxylation at higher processing temperatures.

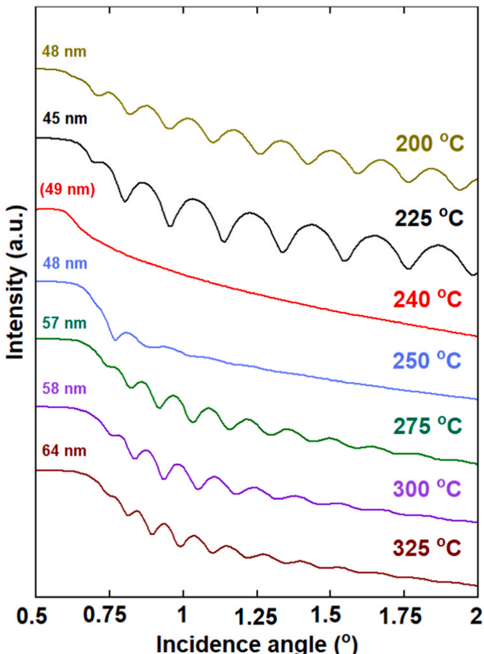

Fig. 5. XRR patterns for the ZrO_2 thin films deposited at various temperatures. The film thickness is indicated on the left; for the 240 °C sample, the thickness value is in parentheses as it was determined by ellipsometry. All other parameters except the deposition temperatures were the same for all samples.

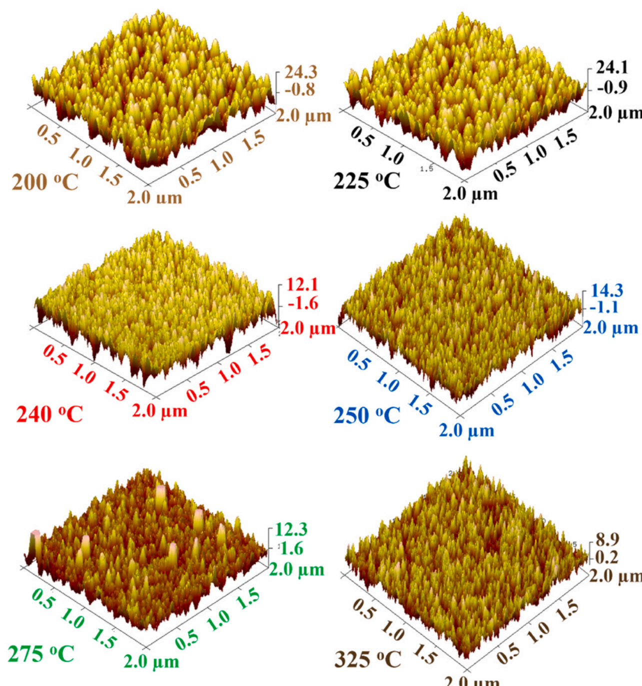

Fig. 6. 3D AFM images for the ZrO_2 thin films deposited at 200, 225, 240, 250, 275, and 325 °C with the short cycle duration scheme and 1000 ALD cycles.

Table 2
Surface roughness of the ZrO_2 thin films deposited at different temperatures with the normal cycle time; the film thicknesses are seen from Fig. 5.

Dep. Temp. (°C) (Dominant phase)	RMS roughness (nm)
200 (o)	2.3
225 (o)	2.4
240 (o)	3.9
250 (o, m*)	4.3
275 (m, o*)	2.8
325 (m, o*)	2.6

* = minor phase

Photoluminescence spectroscopy is widely used to characterize defect states in oxide thin films. In this study, PL measurements were performed on two samples deposited at 240 and 325 °C (Fig. 8). The sample deposited at 240 °C exhibits peaks in the near-UV (350–400 nm) and blue-band (440–470 nm) ranges. The near-UV region is commonly assigned to oxygen-related defects, specifically deep oxygen vacancies (Vo_2) [55–60], while the luminescence in the blue-band range has been attributed to both surface hydroxyl groups and oxygen-related defects (e.g., F-centers) [55,60–65]. Similar features are also observed in the sample deposited at 325 °C. For this reason and given the similar high binding energy oxygen ratios in XPS for 250 and 325 °C samples, we consider it more likely that, in this case, the blue-band emission originates from surface hydroxyl groups. The 325 °C sample, however, lacks the 350–400 nm transitions, while it exhibits a long yellow–green tail after the blue-band peak, extending up to 625 nm. This feature has been associated with both impurities (e.g., Ti and Hf) and shallow oxygen defects (Vo_1) [57,58,65–67]. However, since such impurities are not present, the emission is attributed to shallow oxygen defects. Therefore, the sample deposited at 325 °C, exhibiting both the blue band and the yellow-green tail, is inferred to contain surface hydroxyl groups along with shallow oxygen defects, whereas the 240 °C sample contains

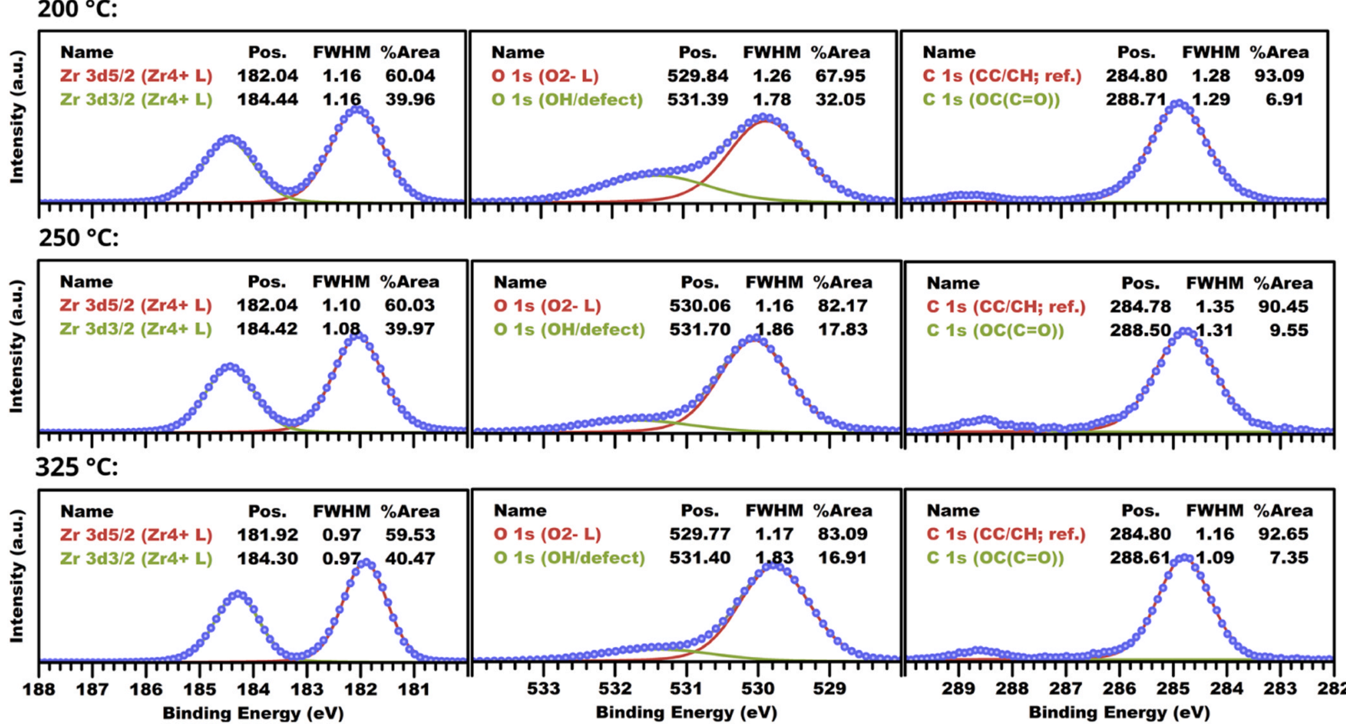

Fig. 7. XPS core-level spectra (left column: Zr 3d, middle: O 1 s, right: C 1 s) for three representative ZrO_2 thin-film samples deposited at 200, 250 and 325 °C, with experimental and fitted data plotted as dotted and solid lines, respectively; the binding energy scale was calibrated using C 1 s at 284.80 eV as a reference.

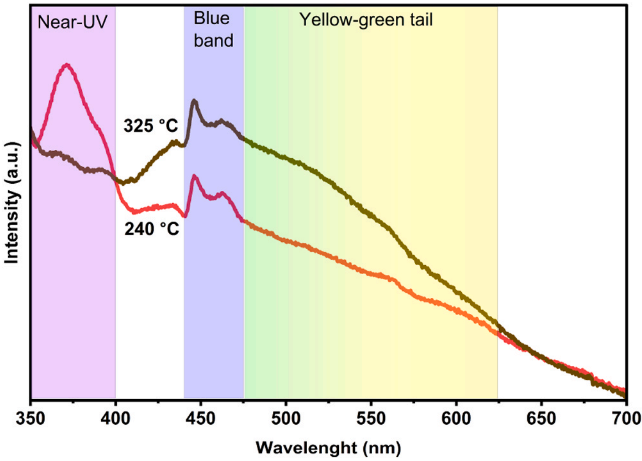

Fig. 8. Photoluminescence spectra of ZrO_2 films deposited at 240 and 325 °C.

surface hydroxyls along with deep oxygen defects. Considering that ZrO_2 can accommodate oxygen defects in both the monoclinic and orthorhombic forms, these findings do not provide definitive evidence regarding the phase type. However, they do indicate that different phases may favor different defect types. Specifically, the orthorhombic phase (sample deposited at 240 °C) appears to favor deep oxygen defects, whereas the monoclinic phase (sample deposited at 325 °C) appears to favor shallow oxygen defects.

3.3. Factors promoting the o-ZrO_2 formation

From previous studies on the polar o-ZrO_2 phase synthesized by various techniques [68–73], the most important factors promoting the formation of this metastable phase seem to be the low synthesis temperature and the existence of oxygen defects (vacancies). Apparently, our ALD CpZr(NMe2)$_3$/H_2O process, yielding nearly phase-pure o-ZrO_2 thin films in the deposition temperature range of 225–250 °C, simultaneously satisfies these factors. Indeed, compared to the other reported ALD processes for crystalline ZrO_2 thin films (not yielding the orthorhombic phase), the present deposition temperature range (225–250 °C) is appreciably low, see Table 1. Also, our process utilizes H_2O as the co-reactant, which is a significantly milder oxidant than the other commonly utilized co-reactants, O_3 and O_2-plasma, and hence more likely to create oxygen vacancies that are believed to have a stabilizing effect on the o-ZrO_2 structure. Finally, the Si/SiO_2 substrate used here could promote the o-ZrO_2 phase formation; a similar facilitating effect of substrate surface on the o-ZrO_2 phase formation was also observed with a Ru sublayer [36]. From Table 1, all the earlier ALD processes reported have missed at least one of the aforementioned factors.

4. Conclusions

We demonstrated a robust water-based ALD process for the fabrication of orthorhombic o-ZrO_2 thin films, using tris(dimethylamino) cyclopentadienyl zirconium as the Zr precursor. The process could be readily optimized regarding the precursor pulse lengths to demonstrate the surface-saturation and growth-linearity behaviors expected for an ideal ALD process. The optimized ALD process with appreciably short precursor pulse lengths (0.6 s for CpZr(NMe2)$_3$ and 0.2 s for H_2O) revealed a so-called ALD or constant-GPC (ca. 0.5 Å/cycle) temperature window of 200–250 °C for the growth of the o-ZrO_2 films, while in the higher deposition temperature range of 275–325 °C the process yielded monoclinic m-ZrO_2 films with a growth rate of 0.6 Å/cycle.

The o-ZrO_2 and m-ZrO_2 thin films distinguishably obtained in the lower and higher deposition temperature ranges, respectively, exhibited – besides the different growth rates and GIXRD patterns – somewhat different XPS and PL spectra presumably due to different oxygen defect types. In particular, the differences seen in the photoluminescence spectra for the ZrO_2 films grown at the lower and higher temperatures reflected the general understanding that the o-ZrO_2 and m-ZrO_2 phases tend to accommodate different types of oxygen defects.

We tentatively attribute our success to fabricate through the CpZr($NMe2)_3$/water process nearly phase-pure thin films of the metastable o-ZrO_2 phase to the significantly low deposition temperature range (225–250 °C) and mild oxygen source (H_2O). These deposition conditions apparently promote the formation of the proper types of oxygen defects (vacancies) that are believed to stabilize the o-ZrO_2 structure.

The GIXRD patterns obtained for all the o-ZrO_2 thin films deposited in the range of 225–250 °C were fully compatible with the space group $Pca2_1$ reported for ferroelectric polar o-ZrO_2. However, with the standard in-house characterization techniques employed in this study it was not possible to rule out the other two space groups (Pbca and Pnma) also reported for o-ZrO_2 in literature. Interestingly, from the deposition experiments in which we increased the ALD cycle time considerably (at deposition temperatures of 230 and 240 °C) we noticed that while the GIXRD patterns were still compatible with the o-ZrO_2 structure (though with a lower degree of crystallinity), the GPC values were lower. Tentatively, we hypothesize that one of the plausible interpretations could be that the shorter ALD cycle time favors the formation of the $Pca2_1$ space group (with larger $V_{f.u}$ and lower density), while with the longer ALD cycle times the structure might relax to the denser (lower $V_{f.u}$) structure with Pbca or Pnma structure. These observations highlight the complexity of the phase stabilization dynamics in ZrO_2 thin films deposited, suggesting a tunable control of the crystal structure via a proper choice of the ALD parameters, in addition to the deposition temperature.

Finally, we like to emphasize that the ALD process developed here possesses the following capabilities in a single process: (1) water-based chemistry, (2) wide and well-defined ALD windows, and (3) distinct temperature ranges yielding different ZrO_2 phases. These capabilities are critical for determining whether a process is suitable for real-world applications. Also importantly, the present ALD-grown o-ZrO_2 thin films were confirmed to be of high-quality, impurity-free, relatively smooth and air-stable, opening thus new opportunities for exploring and exploiting the unique properties of o-ZrO_2, such as the expected ferroelectricity, towards future electronic device applications.

CRediT authorship contribution statement

Basit Ali: Writing – original draft, Visualization, Investigation, Conceptualization. **Ramin Ghiyasi:** Writing – original draft, Validation, Methodology, Investigation, Conceptualization. **Joona Pekkanen:** Writing – review & editing, Investigation. **Mika Lastusaari:** Writing – review & editing, Validation, Resources, Methodology. **Maarit Karppinen:** Writing – original draft, Validation, Supervision, Resources, Funding acquisition, Conceptualization.

Declaration of Competing Interest

The authors declare that they have no known competing financial interests or personal relationships that could have appeared to influence the work reported in this paper.

Acknowledgments

Funding was received from Business Finland CHEMI-SEMI Co-Innovation project and the European Union ERC AdG, UniEn-MLD, No. 101097815. However, the views and opinions shared are solely those of the authors and do not necessarily represent the European Union or the European Research Council. Neither the European Union nor the awarding authority can be held liable for them. We also acknowledge the use of the RawMatTERS Finland Infrastructure (RAMI) at Aalto University, and the provision of facilities and technical support by Aalto University at OtaNano−Microscopy Center (Aalto-NMC). Dr Kristoffer Meinander at Aalto School of Chemical Engineering is thanked for carrying out the XPS measurements.

Appendix A. Supporting information

Supplementary data associated with this article can be found in the online version at doi:10.1016/j.mtcomm.2026.115134.

Data Availability

Data will be made available on request.

References

[1] J. Robertson, High dielectric constant oxides, Eur. Phys. J. 28 (2004) 265–291.
[2] J. Zhao, Y. Wang, Atomic layer deposition of epitaxial ZrO_2 coating on $LiMn_2O_4$ nanoparticles for high-rate lithium ion batteries at elevated temperature, Nano Energy 2 (2013) 882–889.
[3] D. Panda, T.-Y. Tseng, Growth, dielectric properties, and memory device applications of ZrO_2 thin films, Thin Solid Films 531 (2013) 1–20.
[4] C. Meneghini, S. Mobilio, L. Lusvarghi, F. Bondioli, A.M. Ferrari, T. Manfredini, C. Siligardi, The structure of ZrO_2 phases and devitrification processes in a Ca–Zr–Si–O-based glass ceramic: a combined a-XRD and XAS study, Appl. Cryst. 37 (2004) 890–900.
[5] B. Schuster, M. Lang, R. Klein, C. Trautmann, R. Neumann, A. Benyagoub, Structural phase transition in ZrO_2 induced by swift heavy ion irradiation at high-pressure, Nucl. Instr. Methods Phys. Res. B 267 (2009) 964–968.
[6] Y. Zhang, H.-X. Chen, L. Duan, J.-B. Fan, L. Ni, V. Ji, A comparison study of the structural and mechanical properties of cubic, tetragonal, monoclinic, and three orthorhombic phases of ZrO_2, J. Alloy. Comp. 749 (2018) 283–292.
[7] A.H. Heuer, V. Lanteri, S.C. Farmer, R. Chaim, R. Lee, B. Kibbel, R. Dickerson, On the orthorhombic phase in ZrO_2-based alloys, J. Mater. Sci. 24 (1989) 124–132.
[8] A. Sharma, V. Longo, M.A. Verheijen, A.A. Bol, W. Kessels, Atomic layer deposition of HfO_2 using $HfCp(NMe_2)_3$ and O_2 plasma, J. Vac. Sci. Technol. A 35 (2017) 01B130.
[9] S. Consiglio, R.D. Clark, G. Nakamura, C.S. Wajda, G.J. Leusink, Evaluation of high thermal stability cyclopentadienyl Hf precursors with H_2O as a co-reactant for advanced gate logic applications, J. Vac. Sci. Technol. A 30 (2012) 01A119.
[10] E.H. Kisi, C.J. Howard, R.J. Hill, Crystal structure of orthorhombic zirconia in partially stabilized zirconia, J. Am. Cer. Soc. 72 (1989) 1757–1760.
[11] T. Böscke, J. Müller, D. Bräuhaus, U. Schröder, U. Böttger, Ferroelectricity in hafnium oxide thin films, Appl. Phys. Lett. 99 (2011) 102903.
[12] J. Muller, T.S. Boscke, U. Schroder, S. Mueller, D. Brauhaus, U. Bottger, L. Frey, T. Mikolajick, Ferroelectricity in simple binary ZrO_2 and HfO_2, Nano Lett. 12 (2012) 4318–4323.
[13] M.H. Park, Y.H. Lee, H.J. Kim, Y.J. Kim, T. Moon, K.Do Kim, S.D. Hyun, T. Mikolajick, U. Schroeder, C.S. Hwang, Understanding the formation of the metastable ferroelectric phase in hafnia–zirconia solid solution thin films, Nanoscale 10 (2018) 716–725.
[14] X. Li, H. Zhong, T. Lin, F. Meng, A. Gao, Z. Liu, D. Su, K. Jin, C. Ge, Q. Zhang, Polarization switching and correlated phase transitions in fluorite-structure ZrO_2 nanocrystals, Adv. Mater. 35 (2023) 2207736.
[15] Y. Cheng, Z. Gao, K.H. Ye, H.W. Park, Y. Zheng, Y. Zheng, J. Gao, M.H. Park, J.-H. Choi, K.-H. Xue, Reversible transition between the polar and antipolar phases and its implications for wake-up and fatigue in HfO_2-based ferroelectric thin film, Nat. Commun. 13 (2022) 645.
[16] S.S. Cheema, N. Shanker, S.-L. Hsu, Y. Rho, C.-H. Hsu, V.A. Stoica, Z. Zhang, J. W. Freeland, P. Shafer, C.P. Grigoropoulos, Emergent ferroelectricity in subnanometer binary oxide films on silicon, Science 376 (2022) 648–652.
[17] S. Starschich, T. Schenk, U. Schroeder, U. Boettger, Ferroelectric and piezoelectric properties of $Hf_{1-x}Zr_xO_2$ and pure ZrO_2 films, Appl. Phys. Lett. 110 (2017) 182905.
[18] K. Kim, M. Park, H. Kim, Y. Kim, T. Moon, Y. Lee, S. Hyun, T. Gwon, C. Hwang, Ferroelectricity in undoped-HfO_2 thin films induced by deposition temperature control during atomic layer deposition, J. Mater. Chem. C. 4 (2016) 6864–6872.
[19] B. Xu, P.D. Lomenzo, A. Kersch, T. Schenk, C. Richter, C.M. Fancher, S. Starschich, F. Berg, P. Reinig, K.M. Holsgrove, Strain as a global factor in stabilizing the ferroelectric properties of ZrO_2, Adv. Funct. Mater. 34 (2024) 2311825.
[20] J.W. Cho, M.S. Song, I.H. Choi, K.J. Go, J. Han, T.Y. Lee, C. An, H.J. Choi, C. Sohn, M.H. Park, Atomic layer deposition of epitaxial ferroelectric $Hf_{0.5}Zr_{0.5}O_2$ thin films, Adv. Funct. Mater. 34 (2024) 2314396.
[21] T. Suntola, Atomic layer epitaxy, Mater. Sci. Rep. 4 (1989) 261–312.
[22] S.M. George, Atomic layer deposition: an overview, Chem. Rev. 110 (2010) 111–131.
[23] H.H. Sønsteby, A. Yanguas-Gil, J.W. Elam, Consistency and reproducibility in atomic layer deposition, J. Vac. Sci. Technol. A 38 (2020) 020804.
[24] R.W. Johnson, A. Hultqvist, S.F. Bent, A brief review of atomic layer deposition: from fundamentals to applications, Mater. Today 17 (2014) 236–246.
[25] M. Heikkinen, R. Ghiyasi, M. Karppinen, Layer-engineered functional multilayer thin-film structures and interfaces through atomic and molecular layer deposition, Adv. Mater. Interfaces 12 (2025) 2400262.
[26] M. Ritala, M. Leskelä, Zirconium dioxide thin films deposited by ALE using zirconium tetrachloride as precursor, Appl. Surf. Sci. 75 (1994) 333–340.
[27] M. Cassir, F. Goubin, C. Bernay, P. Vernoux, D. Lincot, Synthesis of ZrO_2 thin films by atomic layer deposition: growth kinetics, structural and electrical properties, Appl. Surf. Sci. 193 (2002) 120–128.

[28] J. Aarik, A. Aidla, H. Mändar, T. Uustare, V. Sammelselg, Growth kinetics and structure formation of ZrO_2 thin films in chloride-based atomic layer deposition process, Thin Solid Films 408 (2002) 97–103.
[29] K. Kukli, K. Forsgren, J. Aarik, T. Uustare, A. Aidla, A. Niskanen, M. Ritala, M. Leskelä, A. Hårsta, Atomic layer deposition of zirconium oxide from zirconium tetraiodide, water and hydrogen peroxide, J. Cryst. Growth 231 (2001) 262–272.
[30] M. Putkonen, L. Niinistö, Zirconia thin films by atomic layer epitaxy. A comparative study on the use of novel precursors with ozone, J. Mater. Chem. 11 (2001) 3141–3147.
[31] M. Putkonen, J. Niinistö, K. Kukli, T. Sajavaara, M. Karppinen, H. Yamauchi, L. Niinistö, ZrO_2 thin films grown on silicon substrates by atomic layer deposition with $Cp_2Zr(CH_3)_2$ and water as precursors, Chem. Vap. Dep. 9 (2003) 207–212.
[32] K. Kukli, M. Ritala, M. Leskelä, Low-temperature deposition of zirconium oxide–based nanocrystalline films by alternate supply of $Zr[OC(CH_3)_3]_4$ and H_2O, Chem. Vap. Dep. 6 (2000) 297–302.
[33] R. Matero, M. Ritala, M. Leskelä, A.C. Jones, P.A. Williams, J.F. Bickley, A. Steiner, T. Leedham, H. Davies, Atomic layer deposition of ZrO_2 thin films using a new alkoxide precursor, J. Non-Cryst. Solids 303 (2002) 24–28.
[34] J. Koo, Y. Kim, H. Jeon, ZrO_2 gate dielectric deposited by plasma-enhanced atomic layer deposition method, Jpn. J. Appl. Phys. 41 (2002) 3043.
[35] J. Tong, V. Gopal, I. Hashim, R. Higuchi, A. Lee, Toshiba Corp, SanDisk 3D LLC and Intermolecular Inc, atomic layer deposition of zirconium oxide for forming resistive-switching materials, U.S Patent 8 (741) (2014) 698.
[36] M. Ko, J.S. Park, S. Joo, S. Hong, J.M. Yuk, K.M. Kim, Direct growth of ferroelectric orthorhombic ZrO_2 on Ru by atomic layer deposition at 300° C, Mater. Horiz. 12 (2025) 565–574.
[37] M. Materano, P. Reinig, A. Kersch, M. Popov, M. De Luca, T. Mikolajick, U. Boettger, U. Schroeder, Raman spectroscopy as a key method to distinguish the ferroelectric orthorhombic phase in thin ZrO2-based films, Phys. Status Solidi RRL 16 (2022) 2100589.
[38] E. Choi, H. Kim, S.J. Maeng, J. Lee, D.H. Kim, K. Heo, J.Y. Yun, The effects of decomposition of $CpZr(NMe_2)_3$ on atomic layer deposition for high-k ZrO_2 thin films, Mater. Today Commun. 32 (2022) 104008.
[39] J. Liu, J. Li, J. Wu, J. Sun, Structure and dielectric property of high-k ZrO_2 films grown by atomic layer deposition using tetrakis(dimethylamido)zirconium and ozone, Nanoscale Res. Lett. 14 (2019) 1–12.
[40] G.E. Jellison, F.A. Modine, Parameterization of the optical functions of amorphous materials in the interband region, Appl. Phys. Lett. 69 (1996) 371–373.
[41] A.R. Forouhi, I. Bloomer, Optical properties of crystalline semiconductors and dielectrics, Phys. Rev. B 38 (1988) 1865–1874.
[42] A.R. Forouhi, I. Bloomer, Optical dispersion relations for amorphous semiconductors and amorphous dielectrics, Phys. Rev. B 34 (1986) 7018–7026.
[43] R. Suyama, H. Horiuchi, S. Kume, Structural refinements of ZrO_2 and HfO_2 treated at 600C, J. Ceram. Soc. Jpn. 95 (6) (1987) 567–568.
[44] D.K. Smith, W. Newkirk, The crystal structure of baddeleyite (monoclinic ZrO_2) and its relation to the polymorphism of ZrO_2, Acta Cryst. 18 (1965) 983–991.
[45] R. Ghiyasi, M. Milich, J. Tomko, G.C. Tewari, M. Lastusaari, P.E. Hopkins, M. Karppinen, Simultaneously enhanced electrical conductivity and suppressed thermal conductivity for ALD ZnO films via purge-time controlled defects, Appl. Phys. Lett. 120 (2022) 062106.
[46] J.E. Lowther, J.K. Dewhurst, J.M. Leger, J. Haines, Relative stability of ZrO_2 and HfO_2 structural phases, Phys. Rev. B 60 (21) (1991) 14485–14488.
[47] W.D. Zhang, Z.Z. Song, S.Q. Tang, J.C. Wei, Y. Cheng, B. Li, S.Y. Chen, Z.B. Chen, A.Q. Jiang, Ultrahigh dielectric permittivity in $Hf_{0.5}Zr_{0.5}O_2$ thin-film capacitors, Nat. Commun. 16 (2025) 2679.
[48] A. Ghazy, M. Safdar, M. Lastusaari, M. Karppinen, Amorphous-to-crystalline transition and photoluminescence switching in guest-absorbing metal–organic network thin films, Chem. Commun. 56 (2020) 241–244.
[49] M.Z. Ansari, P. Janicek, Y.J. Park, S. NamGung, B.Y. Cho, D.K. Nandi, Y. Jang, J. S. Bae, T.E. Hong, T. Cheon, W. Song, Preparation of wafer-scale highly conformal amorphous hafnium dioxide thin films by atomic layer deposition using a thermally stable boratabenzene ligand-containing hafnium precursor, Appl. Surf. Sci. 620 (2023) 156834.
[50] C.D. Wagner, A.V. Naumkin, A. Kraut-Vass, J.W. Allison, C.J. Powell, J.R., Rumble, NIST standard reference database 20, Version 3.4 (Web version), National Institute of Standards and Technology, Gaithersburg, MD, 2003, p. 20899.
[51] J.F. Moulder, W.F. Stickle, P.E. Sobol, K.D. Bomben, in: J. Chastain, R.C. King Jr. (Eds.), Handbook of X-Ray Photoelectron Spectroscopy, Perkin-Elmer Corporation, Eden Prairie, MN, 1992, p. 25.
[52] P. Lackner, Z. Zou, S. Mayr, U. Diebold, M. Schmid, Using photoelectron spectroscopy to observe oxygen spillover to zirconia, Phys. Chem. Chem. Phys. 21 (2019) 17613–17620.
[53] G. Beamson, High Resolution XPS of Organic Polymers: The Scienta ESCA300 Database, Wiley, Chichester, 1992.
[54] J.D. Henderson, B.P. Payne, N.S. McIntyre, M.C. Biesinger, Enhancing oxygen spectra interpretation by calculating oxygen linked to adventitious carbon, Surf. Interface Anal. 57 (2025) 214–220.
[55] A.I. Kostyukov, A.A. Nashivochnikov, M.I. Rakhmanova, V.N. Panchenko, A. A. Pochtar, S.V. Cherepanova, V.N. Snytnikov, Photoluminescence of tetragonal ZrO_2 nanoparticles: Contribution from OH groups, oxygen vacancies, and impurities, Opt. Mater. 159 (2025) 116648.
[56] Y. Cong, B. Li, S. Yue, D. Fan, X.J. Wang, Effect of oxygen vacancy on phase transition and photoluminescence properties of nanocrystalline zirconia synthesized by the one-pot reaction, J. Phys. Chem. C. 113 (2009) 13974–13978.
[57] Q. Wang, K. Edalati, Y. Koganemaru, S. Nakamura, M. Watanabe, T. Ishihara, Z. Horita, Photocatalytic hydrogen generation on low-bandgap black zirconia (ZrO_2) produced by high-pressure torsion, J. Mater. Chem. A 8 (2020) 3643–3650.
[58] Z. Wang, J. Zhang, G. Zheng, Y. Liu, Y. Zhao, The unusual variations of photoluminescence and afterglow properties in monoclinic ZrO_2 by annealing, J. Lumin 132 (2012) 2817–2821.
[59] D. Fang, Z. Luo, S. Liu, T. Zeng, L. Liu, J. Xu, Z. Bai, W. Xu, Photoluminescence properties and photocatalytic activities of zirconia nanotube arrays fabricated by anodization, Opt. Mater. 35 (2013) 1461–1466.
[60] K. Smits, L. Grigorjeva, D. Millers, A. Sarakovskis, J. Grabis, W. Lojkowski, Intrinsic defect-related luminescence in ZrO_2, J. Lumin 131 (2011) 2058–2062.
[61] E. Aleksanyan, M. Kirm, E. Feldbach, V. Harutyunyan, Identification of F⁺ centers in hafnia and zirconia nanopowders, Radiat. Meas. 90 (2016) 84–89.
[62] A.S. Vokhmintsev, I.A. Petrenyov, R.V. Kamalov, M.S. Karabanalov, I.A. Weinstein, Thermally stimulated luminescence of oxygen-deficient zirconia nanotubes, J. Lumin 252 (2022) 119412.
[63] Y. Cong, B. Li, B. Lei, W. Li, Long-lasting phosphorescent properties of Ti-doped ZrO_2, J. Lumin 126 (2007) 822–826.
[64] S. Ashraf, M. Irfan, D. Kim, J.H. Jang, W.T. Han, Y.D. Jho, Optical influence of annealing in nano- and submicron-scale ZrO_2 powders, Ceram. Int. 40 (2014) 8513–8518.
[65] T.S. Wang, G.F. Wang, M.L. Qiu, W. Cheng, J.F. Zhang, G.Q. Zhao, The origin of the 500 nm luminescence band related to oxygen vacancies in ZrO_2, J. Lumin 237 (2021) 118133.
[66] X. Yin, Y. Wang, D. Wan, F. Huang, J. Yao, Red-luminescence enhancement of ZrO_2-based phosphor by codoping Eu^{3+} and M^{5+} (M = Nb, Ta), Opt. Mater. 34 (2012) 1353–1356.
[67] K. Smits, L. Grigorjeva, W. Łojkowski, J.D. Fidelus, Luminescence of oxygen-related defects in zirconia nanocrystals, Phys. Status Solidi C. 4 (2007) 770–773.
[68] A.P. Solomon, E.C.O. Quinn, J. Liu, I.M. Gussev, X. Guo, J. Neuefeind, C. Trautmann, R.C. Ewing, G. Baldinozzi, M.K. Lang, Atomic-scale structure of ZrO_2: formation of metastable polymorphs, Sci. Adv. 11 (2025) 5943.
[69] R.M.P. Pereira, M.C. Istrate, F.G. Figueiras, V. Lenzi, B.M. Silva, M. Benamara, K. N. Romanyuk, C. Ghica, B.G. Almeida, L. Marques, M. Pereira, J.P.B. Silva, Phase transitions in ferroelectric ZrO_2 thin films, Mater. Sci. Semicond. Process. 172 (2024) 108102.
[70] A.P.S. Crema, M.C. Istrate, A. Silva, V. Lenzi, L. Domingues, M.O. Hill, V. S. Teodorescu, C. Ghica, M.J.M. Gomes, M. Pereira, L. Marques, J.L. MacManus-Driscoll, J.P.B. Silva, Ferroelectric orthorhombic ZrO_2 thin films achieved through nanosecond laser annealing, Adv. Sci. 10 (2023) 2207390.
[71] G. Baldinozzi, D. Simeone, D. Gosset, M. Dutheil, J. Kusinski, Size-induced tetragonal to monoclinic phase transition in zirconia nanocrystals, MRS Online Proc. Libr. (OPL) 791 (2003) Q5–2.
[72] J. Ouyang, Y. Peng, W. Zhou, X. Liang, G. Wang, Q. Zhang, B. Yuan, The role of oxygen vacancies in phase transition and the optical absorption properties within nanocrystalline ZrO_2, Nanomater 14 (2024) 967.
[73] B. Xu, L. Collins, K.M. Holsgrove, T. Mikolajick, U. Schroeder, P.D. Lomenzo, Influence of the ozone dose time during atomic layer deposition on the ferroelectric and pyroelectric properties of 45 nm-thick ZrO_2 films, ACS Appl. Electron Mater. 5 (2023) 2288–2295.